ACS APPLIED MATERIALS & INTERFACES

Research Article

www.acsami.org

Quantum Chemical Design of Doped $Ca_2MnAlO_{5+\delta}$ as Oxygen Storage Media

Chen Ling,* Ruigang Zhang, and Hongfei Jia

Toyota Research Institute of North America, 1555 Woodridge Avenue, Ann Arbor, Michigan 48105, United States

Supporting Information

ABSTRACT: Brownmillerite Ca_2MnAlO_5 has an exceptional capability to robustly adsorb half-molecules of oxygen and form $Ca_2MnAlO_{5.5}$. To utilize this unique property to regulate oxygen-involved reactions, it is crucial to match the oxygen release−intake equilibrium with targeted reaction conditions. Here we perform a comprehensive investigation of the strategy of tuning the oxygen storage property of Ca_2MnAlO_5 through chemical doping. For undoped $Ca_2MnAlO_{5+\delta}$, our first-principles calculation predicts that the equilibrium temperature at a pressure of 1 atm of O_2 is 848 K, which is in excellent agreement with experimental results. Furthermore, the doping of alkaline earth ions at the Ca site, trivalent ions at the Al site, and 3d transition metal ions at the Mn site is analyzed. By the doping of 12.5% of Ga, V, and Ti, the equilibrium temperature shifts to high values by approximately 110−270 K, while by the doping of 12.5% of Fe, Sr, and Ba, the equilibrium temperature is lowered by approximately 20−210 K. The doping of these elements is thermodynamically stable, and doping other elements including Mg, Sc, Y, Cr, Co, and Ni generates metastable compounds. The doping of a higher content of Fe, however, lowers the oxygen storage capacity. Finally, on the basis of our calculated data, we prove that the formation energetics of nondilute interacting oxygen vacancy in doped $Ca_2MnAlO_{5.5}$ scale linearly with a simple descriptor, the oxygen p-band position relative to the Fermi level. The higher-oxygen p-band position leads to a lower vacancy formation energy and thus a lower oxygen release temperature. Understanding such a relationship between fundamental quantum chemical properties and macroscopic properties paves the road to the design and optimization of novel functional oxides.

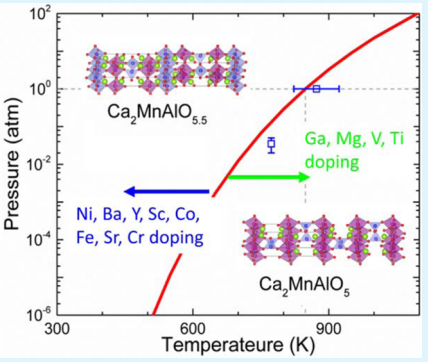

KEYWORDS: *oxygen storage material, brownmillerite, Ca_2MnAlO_5, $Ca_2MnAlO_{5.5}$, chemical doping*

INTRODUCTION

Many transition metal oxides are capable of changing oxygen stoichiometry with the variation of temperature or oxygen partial pressure. This property leads to the concept of oxygen storage materials (OSMs), where large amounts of oxygen can be reversibly stored and released. Because of their ability to regulate oxygen pressure, OSMs have great potential in applications such as heterogeneous catalysts and three-way catalysts.[1−5] In these applications, an efficient OSM certainly should have a large oxygen storage capacity, fast release and storage rate, and good stability against thermal or chemical decomposition.[6] Another crucial property of OSMs is the temperature and pressure for the switch between oxygen-rich and -poor phases, usually determined by the thermodynamic equilibrium between the oxidized (oxygen-rich) and reduced (oxygen-poor) phase and the kinetics of the intake and release of oxygen. As illustrated in Figure 1, to provide the necessary functionality, the intake and release of oxygen must occur at the same conditions in which the targeted reaction proceeds. Thermodynamically, a desirable OSM should have its equilibrium pressure−temperature ($P-T$) curve crossing the window of temperatures and pressures where the reaction conditions fluctuate. Therefore, it is essential to tune the equilibrium $P-T$ curve to match the operating conditions for different applications.

Recently, Ca_2MnAlO_5 with a brownmillerite-type structure was reported with a remarkable capability for storing a large amount of excess oxygen.[5] Its oxygen storage capability (2006 μmol/g) is over 1.3 times that of the best-known OSM, CeO_2-ZrO_2 (approximately 1500 umol/g). In contrast to the case of CeO_2-ZrO_2, which only releases oxygen under reductive conditions, $Ca_2MnAlO_{5+\delta}$ is capable of releasing oxygen under oxygen-rich atmospheres with high sensitivity to the small variation of temperatures.[5] These characteristic features suggest the good potential of $Ca_2MnAlO_{5+\delta}$ in oxygen-storage technologies. However, $Ca_2MnAlO_{5+\delta}$ intakes and releases oxygen only in a narrow temperature range between 500 and 700 °C,[5] which would limit its application in reactions outside of this temperature window.

One effective way to tune the properties of functional materials is through well-designed chemical doping. Prior research work has applied this strategy successfully in several OSMs. For instance, for oxygen storage in CeO_2, an enhanced

Received: May 11, 2015
Accepted: June 11, 2015
Published: June 11, 2015

DOI: 10.1021/acsami.5b03729
ACS Appl. Mater. Interfaces 2015, 7, 14518−14527

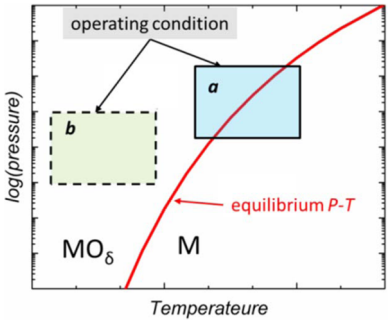

Figure 1. Schematic of the equilibrium between the oxidized phase (MO_δ) and reduced phase (M) of an oxygen storage material and of the operating window of the targeted reaction. In case a, the equilibrium $P-T$ curve crosses the operation window, suggesting that the oxygen storage material can function in the entire range. In case b, the equilibrium curve does not cross the operation window. In this case, the oxygen storage material stays at the oxygen-rich phase without any functionality during the operation.

oxygen storage capacity was achieved by replacing Ce^{4+} with isoelectronic ions such as Zr^{4+}, Ti^{4+}, and Sn^{4+}.[7−9] It was shown that adding zirconia to ceria greatly enhances the reducibility of the Ce^{4+} ion.[8] By the varying of the Zr concentration in the CeO_2-ZrO_2 solid solution, the peak temperature for the oxygen release reaction was controlled from 1200 to 500 K, which covered a large temperature range for the three-way catalyst. In the study of $YBaCo_4O_7$, the low-temperature oxygen storage capability highly depended on the choice of dopants. The oxygen release temperature decreased with the ionic size of the rare earth constituent,[10] and the temperature for the thermal decomposition was increased by doping at the Y or Ba site with smaller cations or doping at the Co site with Al and Ga.[6,10] For $Dy_{1-x}Y_xMnO_{3+\delta}$, the oxygen storage capacity, adsorption rate, and the temperature to release oxygen all decrease with the increasing yttrium content.[11]

In search of appropriate dopants for complex oxides is, however, not trivial. It requires carefully optimized synthesis to avoid the formation of impurities. In addition, the dopant may not be thermodynamically feasible for substituting in the host structure, which increases the challenge to obtain desirable product. For these reasons, a theoretical investigation is greatly instructive to guide any experimental efforts. In the current work, we explore the possibility of tuning the oxygen storage property of $Ca_2MnAlO_{5+\delta}$ with well-designed chemical doping. Equipped with first-principles calculation, we start with a comprehensive mechanistic analysis of oxygen storage in pristine $Ca_2MnAlO_{5+\delta}$. After that, we focus on investigating an isoelectronic doping strategy that includes divalent alkaline earth ions doping at the Ca site, trivalent Ga^{3+}, Sc^{3+}, and Y^{3+} ions doping at the Al site, and 3d transition metal ions doping at the Mn site. The oxygen storage and release thermodynamics are analyzed, and feasible doping strategies that effectively tune the equilibrium temperature by as much as −210 to +270 K are proposed. On the basis of our calculated data, we rationalize the fundamental principle behinds the calculated oxygen storage and release energetics, the knowledge of which benefits future experimental explorations. Perspective about the applications of $Ca_2MnAlO_{5+\delta}$ is also discussed in the last section.

METHODS

Reaction Enthalpy, Free Energy, and Substitutional Energy. We are interested in calculating the enthalpy and free energy of the oxygen release reaction

$$MO_{5.5} \rightarrow MO_5 + 0.25O_2 \quad (1)$$

where MO_5 represents the chemically doped Ca_2MnAlO_5, and $MO_{5.5}$ represents $Ca_2MnAlO_{5.5}$. Here we treat the release oxygen as gaseous O_2, the same condition as in the report of Motohashi et al.[5] If cycles such as H_2/H_2O or CO/CO_2 are used to release and intake oxygen, similar procedures to predict the equilibrium temperature can be carried out by rewriting reaction 1. The temperature-dependent Gibbs free energy of reaction 1 is

$$\Delta G = \left(H_{MO_5} - H_{MO_{5.5}}\right) - T\left(S_{MO_5} - MO_{5.5}\right) + 0.25G_{O_2} \quad (2)$$

Because the volume change in the solid component is small relative to the volume change associated with releasing gaseous O_2, the PV contribution due to changes in the volumes of the solid phases can be neglected. The free energy of O_2 gas is related to the temperature and pressure by

$$G_{O_2}(T,P) = H_{O_2}(T) - TS_{O_2}(T) + kT\ln(P/P^0) \quad (3)$$

To overcome the inaccuracy in calculating the binding energy of O_2, we adapt a correction to the oxygen bonding energy as recommended in ref 12. With this correction, the reaction enthalpy at 300 K is

$$\Delta H_{300} \simeq E_{MO_5} - E_{MO_{5.5}} + 0.25E^*_{O_2} \quad (4)$$

At temperature T, the enthalpy is obtained as

$$\Delta H(T) = \Delta H_{300} + 0.25H_{O_2}(T) - 0.25H_{O_2}(300\,\mathrm{K}) \quad (5)$$

The Gibbs free energy is

$$\Delta G(T) = \Delta H(T) - T\left(S_{MO_5} - S_{MO_{5.5}}\right) + 0.25TS_{O_2}(T) + 0.25kT\ln(P/P^0) \quad (6)$$

Density functional theory (DFT) was used to calculate the energies of the $MO_{5.5}$ and MO_5 phases with and without chemical dopant. The experimental values were used for the standard enthalpy and entropy of O_2 gas. The standard way to take into account the entropy of the solid is to explicitly evaluate the phonon contribution to the vibrational entropy.[13] This approach is much more expensive in comparison to the cost of energy minimizations. Considering that MO_5 and $MO_{5.5}$ have complex but rather similar crystal structures (see the next section), we make the approximation that the entropy difference between $MO_{5.5}$ and MO_5 is mainly contributed by the harmonic vibration of excess oxygen in the $MO_{5.5}$ phase. With this approximation, we obtain[13]

$$S_{MO_5} - S_{MO_{5.5}} = k_b \sum\left[-\ln(1 - e^{-\beta h\nu}) + \beta h\nu/(e^{\beta h\nu} - 1)\right] \quad (7)$$

where k_b, h, and ν are the Boltzmann constant, Planck constant, and the vibrational frequency of excess oxygen ions, respectively. The summation runs on all vibrational frequencies and $\beta = 1/k_bT$.

To analyze the thermodynamic feasibility of chemical doping, we evaluate the formation energy of chemical-doped $Ca_2MnAlO_{5+\delta}$. Using Kröger−Vink notation, the substitution of isoelectronic dopant is expressed as

$$X + Y_Y^\times \rightarrow X_Y^\times + Y \quad (8)$$

The substitution formation energy is defined as

$$E_{sub} = E_{X_Y^\times} - E_{Y_Y^\times} + \mu_Y - \mu_X \quad (9)$$

where $E_{X_y^\times}$ and $E_{Y_y^\times}$ are the energy of chemical-doped and undoped $Ca_2MnAlO_{5+\delta}$, respectively. The values μ_Y and μ_X represent the chemical potentials of Y and X in the reference state, respectively. The substitution energy shown in reaction 8 depends on the choice of

DOI: 10.1021/acsami.5b03729
ACS Appl. Mater. Interfaces 2015, 7, 14518−14527

reference state in the calculation. Consider that the synthesis of Ca_2MnAlO_5 is typically carried out by calcinating the mixture of its parent oxides. The most natural way is to use the oxide format as the reference state for X and Y.[14] Therefore, AO is used as the reference state for alkaline earth ions, where A represents the cation. For trivalent ions, we used A_2O_3 as the reference state. Because the oxidation state for Mn is 3+ in Ca_2MnAlO_5, A_2O_3 is also used as the reference state for 3d transition metal ions. However, Ni and Co do not have known stable A_2O_3 oxides. Therefore, we use the corrected reference states as[14]

$$A_2O_3^* = \left(\frac{2}{3}Co_3O_4 + \frac{1}{6}O_2\right), (2NiO + 0.5O_2) \quad (10)$$

With the use of these reference states, the substitution energy represents the free energy change (300 K) by forming doped $Ca_2MnAlO_{5+\delta}$ from a mixture of pure $Ca_2MnAlO_{5+\delta}$ and dopant oxide. A negative substitution energy indicates thermodynamically favorable doping, and a positive value indicates unfavorable doping.

Crystal Structure. Ca_2MnAlO_5 crystallizes in a brownmillerite structure,[15,16] a defective perovskite with ordered oxygen vacancies. The larger Ca ion is located at the perovskite A site, and the smaller Mn and Al ions occupy the perovskite B site and stack alternately, resulting in a MnO_6−Ca−AlO_4−Ca layered stacking order as illustrated in Figure 2a. By accepting the excess oxygen in the lattice,

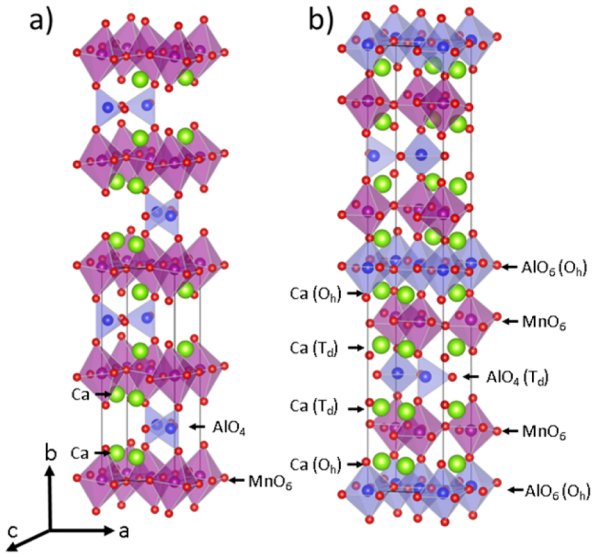

Figure 2. Crystal structures of brownmillerite (a) Ca_2MnAlO_5 (space group *Ibm2*) and (b) $Ca_2MnAlO_{5.5}$ (space group *Imma*). Red, oxygen; blue, Al; purple, Mn; green, Ca.

the half-tetrahedral AlO_4 changes the coordination and becomes octahedral AlO_6 in $Ca_2MnAlO_{5.5}$, resulting in a MnO_6−Ca−AlO_4−Ca−MnO_6−Ca−AlO_6 stacking order (Figure 2b).[17] The octahedral- and tetrahedral-bonded Al ions are distinguished as Al_O_h and Al_T_d, respectively. Similarly, Ca between the Al_O_h and Mn layer is named as Ca_O_h, and Ca between the Al_T_d and Mn layer is named as Ca_T_d.

Ca_2MnAlO_5 crystallizes in the space group *Ibm2*,[15,16] and $Ca_2MnAlO_{5.5}$ crystallizes in the space group *Imma*.[17] These experimental structures were used as the initial inputs in DFT relaxations. The reported structure of $Ca_2MnAlO_{5.5}$ contains half-occupied Al_T_d and oxygen sites.[17] We first estimated the electrostatic energy for all possible occupancies in a unit cell by assigning formal charges (Ca, +2; Mn, 4+; Al, +3; O, −2) in the Ewald summation and performed DFT calculations for the structure with the lowest electrostatic energy. The atomic coordinates for the relaxed structure of Ca_2MnAlO_5 and $Ca_2MnAlO_{5.5}$ are listed in Tables S2 and in the Supporting Information.

DFT Calculations. DFT calculations were performed using the Vienna ab initio simulation package (VASP) with projector augmented waves (PAW) pseudopotentials and the exchange-correlation functional parametrized by Perdew, Burke, and Ernzerhof for the generalized gradient approximation (GGA).[18−20] To describe the d-part of the Hamiltonian, the GGA + U method was used for 3d transition metal ions, with the U parameter optimized as in reference 12. A cutoff energy of 500 eV was used with 6 × 2 × 6 γ-centered k-point mesh for the unit cell of the O_5 phase and 6 × 1 × 6 for the unit cell of the $O_{5.5}$ phase. With these settings, the numerical convergence was ensured to less than 2 meV per formula unit. In all calculations, the relaxation was first performed on the ionic positions and the unit cell size. The final energy of the optimized structure was recalculated to avoid any error caused by the changes in the basis set of the wave functions. To study the migration of oxygen ions, we applied the climb-nudged elastic band method in the search for transition states.[21,22]

RESULTS

Oxygen Storage in Ca_2MnAlO_5. We begin with the calculation for undoped Ca_2MnAlO_5. Table 1 lists the DFT-optimized lattice parameters for Ca_2MnAlO_5 and $Ca_2MnAlO_{5.5}$. These calculated values are very close to the experimental data, which is also included for comparison.[15,17] The unit cell volume is slightly overestimated by 1−4%, which is a common trend for GGA-based calculations.

Table 1. Lattice Parameters of $Ca_2MnAlO_{5+\delta}$ (δ = 0 and 0.5)

	Ca_2MnAlO_5		$Ca_2MnAlO_{5.5}$	
	DFT	experimental[15]	DFT	experimental[17]
a (Å)	5.601	5.469	5.291	5.286
b (Å)	15.007	15.003	29.696	29.533
c (Å)	5.337	5.243	5.451	5.403
V (Å^3)	448.6	430.1	856.6	843.4

The unit cell of $Ca_2MnAlO_{5.5}$ contains 44 oxygen ions at six symmetrically distinct positions.[17] A series of calculations was carried out to examine the stable structure after the removal of oxygen atoms. In the first step, we considered taking out one oxygen atom at each possible site. Table 2 lists the oxygen vacancy formation enthalpy at 300 K. Vacancy prefers to form in the Al_O_h layer, followed by the formation in the Ca_O_h layer. In these two layers, oxygen ions are bonded to AlO_6 octahedra. The removal of oxygen from the AlO_4 tetrahedra (Al_T_d and Ca_T_d layers) has the highest formation enthalpy. This result strongly suggests that the release of oxygen from $Ca_2MnAlO_{5.5}$ decreases the coordination number of octahedrally bonded Al ions. In the next step, the removal of two oxygen ions from one Al_O_h layer was considered. The enthalpy to form oxygen divacancy is smaller than that of the

Table 2. Enthalpy to Form Oxygen Vacancy in $Ca_2MnAlO_{5.5}$

configuration	position	H_f (eV)
monovacancy	Al_O_h layer	1.66
	Ca_O_h layer	1.72
	Mn layer	2.66
	Mn layer	2.74
	Ca_T_d layer	4.82
	Al_T_d layer	6.45
divacancy	[100]	2.24
	[001]	2.29
	[101]	2.44

DOI: 10.1021/acsami.5b03729
ACS Appl. Mater. Interfaces 2015, 7, 14518−14527

formation of two isolated single vacancies by approximately 1.1 eV. The most stable configuration has oxygen divacancy preferably oriented along the [100] or [001] direction rather than the [101] direction. Perovskite with oxygen vacancy ordering in this way usually has cations tetrahedrally bonded.[23] Interestingly, this is also the same trend found in the experiments, in which Al_O_h changes from octahedral bonding to tetrahedral bonding with the composition changes from $Ca_2MnAlO_{5.5}$ to Ca_2MnAlO_5.

Each unit cell of $Ca_2MnAlO_{5.5}$ contains two Al_O_h layers. The enthalpy for the formation of one oxygen divacancy in each layer (four oxygen vacancies in one unit cell) was also examined. Without performing any reorientation of the undercoordinated Al polyhedra, the DFT relaxation converged in a local minimum with a formation enthalpy of 4.50 eV. For the experimentally reported Ca_2MnAlO_5 structure, the undercoordinated Al polyhedral is deformed into the tetrahedral bonding, which reduced the formation enthalpy by 1.17 eV. Therefore, the reaction enthalpy is 0.417 eV (+40.2 kJ/mol) for the reaction

$$Ca_2MnAlO_{5.5} \rightarrow Ca_2MnAlO_5 + 0.25O_2 \quad (11)$$

With this enthalpy value, we proceeded to obtain an equilibrated $P-T$ curve using eq 6. Figure 3 shows the

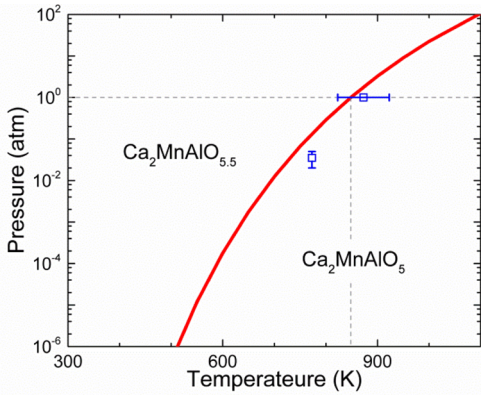

Figure 3. Temperature-dependent equilibrium pressure between $Ca_2MnAlO_{5.5}$ and Ca_2MnAlO_5 as obtained from first-principles calculations (red) in comparison with experimental data (blue) from ref 5.

calculated equilibrium temperature as a function of the O_2 partial pressure. The predicted $P-T$ curve agrees with the experimental measurements excellently. At an O_2 pressure of 1 atm, our DFT analysis gave the transition temperature at 848 K, and the experimental measurements showed an average value around 873 K.[5] Although the agreement in this level suggests the power of DFT calculation in the study of OSMs, we point out that it is necessary to include the vibrational contribution to the free energy in the calculation. Without this contribution, the calculated transition temperature shifted by approximately 50 K.

The excellent agreement between the DFT-predicted $P-T$ curve and the experimental measurements implies the oxygen storage property of $Ca_2MnAlO_{5+\delta}$ is mainly determined by thermodynamics rather than kinetics; otherwise, the experimentally measured oxygen release and intake should deviate significantly from the calculated thermodynamic equilibrium. To support this hypothesis, we evaluated the mobility of oxygen vacancy in $Ca_2MnAlO_{5.5}$. A rapid release and intake of oxygen requires fast oxygen diffusion through the lattice.[24,25] The mobility of oxygen vacancy therefore provides quantitative information about the kinetics of oxygen release. Figure 4a

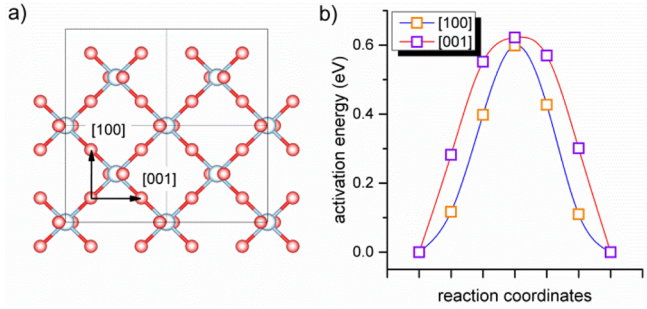

Figure 4. Diffusion of oxygen vacancy in $Ca_2MnAlO_{5.5}$. (a) Schematic of the diffusion along the [100] and [001] directions in an octahedral-bonded Al layer. Blue, Al; red, oxygen. (b) Energy profile for the diffusion from first-principles calculations.

examines the diffusion path way of oxygen on one Al_O_h layer. The diffusion barrier is 0.60 and 0.62 eV along [100] and [001] direction, respectively (Figure 4b). The diffusion is slightly faster along the [100] direction, but the difference is nearly negligible. The calculated diffusion barrier is within the range of 0.4−0.8 eV that has been reported for many perovskite oxides used as solid oxide fuel cell cathodes.[26−28] It is also comparable to the diffusion in other OSMs such as $BaYMnO_6$, which has a barrier of approximately 0.70 eV.[29] These comparisons imply that the mobility of oxygen vacancy in $Ca_2MnAlO_{5.5}$ is sufficient to support quick-release kinetics. Indeed, it was observed experimentally that the release of oxygen happens nearly without any noticeable hysteresis once the operating conditions (temperature or O_2 partial pressure) shifts.[5] The heated Ca_2MnAlO_5 starts to adsorb oxygen in the lattice around 200 °C, implying considerable oxygen mobility at this temperature.[5] Thus, for the release of oxygen from $Ca_2MnAlO_{5.5}$ at higher temperatures, it is the thermodynamics instead of the kinetics that determines the decomposition temperature.

Before we proceed to the next section, we present a discussion of the role of Mn and Al to the oxygen release and intake property. They both occupy the B site in the perovskite ABO_3 compound but functionalize completely differently. The major function of Mn is to provide a redox center that is capable of tuning its valence to balance the electron neutrality. In the release of oxygen, Mn^{4+} is reduced to Mn^{3+} and vice versa. If we replace Mn with a redox-inactive species such as Al, the oxidized form ($Ca_2Al_2O_{5.5}$) is greatly destabilized with a substitutional energy of 0.73 eV. It is easy to understand because Al is inert to change its oxidation state to 4+. Substituting Al for Mn decreases the amount of redox active ions, which therefore results in a lower oxygen storage capacity. This is supported by the experimental evidence that the capacity of $Ca_2Mn_{1-x}Al_{1+x}O_5$ gradually decreased with the increase in x value.[5]

The presence of Al provides a lattice that can robustly vary its coordination number. The importance of having Al can be verified by replacing Al with Mn ions, the latter of which prefers the O_h site in brownmillerite structures.[30] In the reduced $Ca_2Mn_2O_5$, Mn ions that replace Al are tetrahedrally bonded. As a result, it has a high substitutional energy of 0.47 eV. In the oxidized $Ca_2Mn_2O_{5.5}$, only half of the Mn ions that replace Al ions are tetrahedrally bonded, while the other half are still

DOI: 10.1021/acsami.5b03729
ACS Appl. Mater. Interfaces 2015, 7, 14518−14527

octahedrally bonded. Consequently, the substitutional energy for forming $Ca_2Mn_2O_{5.5}$ is reduced to 0.04 eV, much less than that for $Ca_2Mn_2O_5$. These results suggest that to have a robust capability for reversibly adsorbing and releasing oxygen, it is critical to contain a species that can vary its local coordination number without disturbing the whole crystal structure.

Oxygen Storage in Chemical-Doped $Ca_2MnAlO_{5+\delta}$. We are now positioned to study the oxygen storage property of chemical-doped $Ca_2MnAlO_{5+\delta}$. Specifically, we consider isovalent doping at the Ca, Mn, and Al sites. These include the doping of alkaline earth ions (Mg, Sr, and Ba) at the Ca site, the doping of trivalent ions (Ga, Sc, and Y) at the Al site, and the doping of 3d transition metal (Ti to Ni; Cu is not included as it hardly goes to Cu^{4+}) at the Mn site. We note that some dopants may possibly occupy different lattice sites during the synthesis. This possibility is not considered in current work. Table 3 lists the calculated reaction enthalpy and the transition temperature at the 1 atm O_2 partial pressure. These results are discussed in detail on the basis of the doping sites. ‘

Table 3. Reaction Enthalpy (ΔH_{300}, eV) and Transition Temperature at 1 atm O_2 Partial Pressure (T_c, Kelvin) for Chemical-Doped $Ca_2MnAlO_{5+\delta}$

site	doping element	ΔH_{300}	T_c
undoped	–	0.417	848
Ca	Mg	0.468	964
	Sr	0.407	827
	Ba	0.324	641
	Ga	0.465	958
Al	Sc	0.354	708
	Y	0.325	644
Mn	Ti	0.544	1121
	V	0.530	1103
	Cr	0.420	854
	Fe	0.387	781
	Co	0.364	729
	Ni	0.242	463

Alkaline Earth Ion Doping at the Ca Site. The unit cell of $Ca_2MnAlO_{5.5}$ contains two symmetrically distinct Ca sites that are distinguished by their distances to Al_O_h and Al_T_d layers.[17] DFT calculations reveal that the replacement of Ca with larger Sr or Ba preferably happens at the Ca_O_h site. The doping of Sr and Ba at the Ca_T_d site is energetically unstable by 0.81 and 1.23 eV, respectively. On the contrary, doping of Mg is more stable at the Ca_T_d site, and the energy of the configuration with Mg at the Ca_O_h site is 0.82 eV higher.

It can be seen from Table 1 that the size of the dopant at the Ca site also greatly affects the reaction enthalpy. Doping large alkaline earth ions decreases the reaction enthalpy, thus lowering the transition temperature. Such a trend is understood because the lattice expansion caused by the replacement of Ca with larger alkaline earth ions weakens the oxygen bonding strength; therefore, the release of oxygen is energetically easier for a larger dopant.[31] To quantitatively illustrate this trend, in Figure 5 we plotted the reaction enthalpy against the relaxed alkaline earth−oxygen bond distances. An apparently large alkaline earth−oxygen bond length leads to a lower reaction enthalpy. From Mg to Sr, the reaction enthalpy gradually decreases by 0.07 eV. Accordingly, doping Mg increases the transition temperature by approximately 120 K, and doping Sr slightly decreases the transition temperature. The decrease of

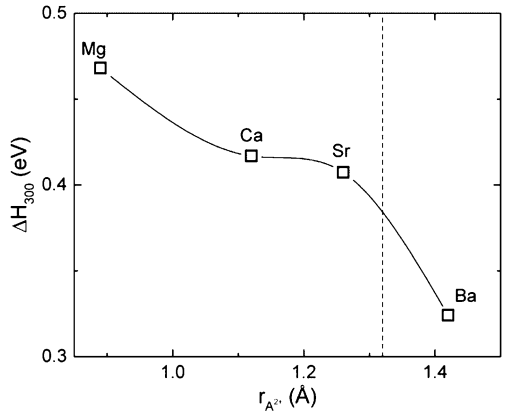

Figure 5. Oxygen-release enthalpy at 300 K for alkaline-earth-doped $Ca_2MnAlO_{5.5}$ as a function of the radius of the alkaline ions. The dotted line shows the critical ionic radius to occupy the A site in a perovskite-based structure with the B site occupied by Mn and Al.

reaction enthalpy is more obvious for Ba doping. For an ideal perovskite ABO_3 structure, the bond lengths satisfy $r_A + r_o = \sqrt{2}(r_b + r_o)$. For the oxygen-rich phase, the ideal radius at the A site is estimated to be 1.32 Å, which is far below the ionic size of Ba^{2+} (1.42 Å).[32] Therefore, the doping of large Ba ions destabilizes the oxygen-rich phase. As a result, the reaction enthalpy quickly drops by 0.17 eV from the Sr to Ba doping. The transition temperature for Ba-doped $Ca_2MnAlO_{5+\delta}$ drops by approximately 200 K.

Trivalent Ion Doping at the Al Site. The unit cell of $Ca_2MnAlO_{5.5}$ contains two symmetry-distinct Al sites bonded in octahedral and tetrahedral environments. DFT calculations showed that the doping of Ga at the Al_O_h site is more stable by 0.13 eV, which implies the preference of Ga to stay with octahedral bonding. As a consequence of this site preference, the replacement of Al by Ga destabilizes the reduced phase, in which the doped Ga has to stay in the tetrahedral environment. The reaction enthalpy is increased by approximately 0.10 eV, and the transition temperature is increased by approximately 110 K.

The doping of even larger trivalent ions is also investigated in the current study. The ionic sizes of Sc^{3+} (0.87 Å) and Y^{3+} (0.90 Å) are 63% and 68% larger than that of Al^{3+} (0.535 Å).[32] As we show later, such a large size mismatch destabilizes the doped compound, especially for the oxidized $O_{5.5}$ phase, whose unit cell size is smaller than the reduced O_5 phase. As a result, the doping of Sc and Y lowers the transition temperature by 140 and 204 K, respectively.

3d Transition Metal Doping at the Mn Site. The release of oxygen from $Ca_2MnAlO_{5.5}$ requires the distribution of one extra electron on the lattice. As shown earlier, the function of Mn is to provide an active redox center that tunes the valence to balance the charge transfer. Therefore, the oxidation and reduction of the transition metal ions directly affect the reaction enthalpy. In Table 3, the reaction enthalpy generally decreases from early 3d transition metals (Ti and V) to late transition metals (Co and Ni). Compared to the undoped $Ca_2MnAlO_{5+\delta}$, the doping of Ti and V increases the transition temperature by 273 and 255 K, respectively. Additionally, to the contrary, the doping of 12.5% of Fe, Co, and Ni decreases the transition temperature by 67, 119, and 205 K, respectively.

Xiao et al. showed that the stability of oxygen vacancy in a transition-metal-doped-layered, Li-rich layered oxide (Li_2MO_3)

DOI: 10.1021/acsami.5b03729
ACS Appl. Mater. Interfaces 2015, 7, 14518−14527

was affected by the degree of covalency of the transition metal−oxygen bond.[33] Oxygen ions are easy to remove when the electrons are less localized in a relatively more covalent bond. However, as shown earlier, the oxygen released from $Ca_2MnAlO_{5.5}$ does not bond directly to the transition metal ions. Therefore, it is the transition metal redox potential instead of the transition metal−oxygen bond strength that directly affects the oxygen vacancy stability. Consider the release of oxygen as the cleavage of the bonding of the target oxygen ions and the consequent reduction of the transition metal ions from TM^{4+} to TM^{3+}. The reaction enthalpy of these processes can be correlated to the TM cation reduction exothermicities.[34] Indeed, experimental TM^{3+} ionization potentials nicely correlate the computed reaction enthalpy as shown in Figure 6. Those TM^{3+} ions with larger IPs exhibit higher ΔH values,

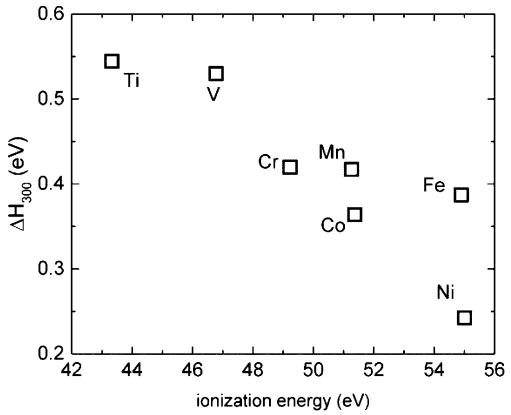

Figure 6. Enthalpy for the release of oxygen from 3d-transition-metal-doped $Ca_2MnAlO_{5.5}$ versus the ionization energy of the transition metal from the 3+ to the 4+ oxidation state.

indicating they are more reluctant to be oxidized. The only ion that seems to deviate from this general trend is Fe^{3+}. This is probably because Fe^{4+} can be better stabilized in certain brownmillerite structures.[35] As a result, the reaction enthalpy for the Fe-doped compound is less than expected.

Effect of Codoping of Two Elements. The effect of codoping of two elements is also considered in our study. We select two examples: the codoping of Ba and Fe, because both elements lower the reaction enthalpy, and the codoping of Ga and Ti, because both elements increase the reaction enthalpy. The reaction enthalpies and transition temperatures are listed in Table 4. Compared to reaction enthalpy of the doping of a

Table 4. Reaction Enthalpy (ΔH_{300}, eV) and Transition Temperature at 1 atm O_2 Partial Pressure (T_c, Kelvin) for $Ca_2MnAlO_{5+\delta}$ Codoped with Two Elements

element 1	element 2	ΔH_{300}	T_c
Ba	Fe	0.314	618
Ga	Ti	0.554	1131

single element, the reaction enthalpy changes more for the codoped $Ca_2MnAlO_{5+\delta}$. However, we should also see that the codoping cannot be simply treated as a cumulative effect of single element doping. For instance, the codoping of Ba and Fe only lowers the reaction enthalpy by 0.103 eV, about 16% less than the sum of the reaction enthalpy of Ba-doped and Fe-doped $Ca_2MnAlO_{5+\delta}$. It suggests the possible interaction between the codopant also plays a role in affecting the reaction enthalpy. A similar trend is also observed for Ga−Ti codoping. The doping of Ga and Ti increases the reaction enthalpy by 0.048 and 0.127 eV, and the codoping increases the reaction enthalpy by 0.138 eV.

Feasibilities of Chemical Doping. We turn our attention to the feasibility of doping analyzed in the current work. Figure 7 shows the calculated substitutional enthalpies for both the O_5

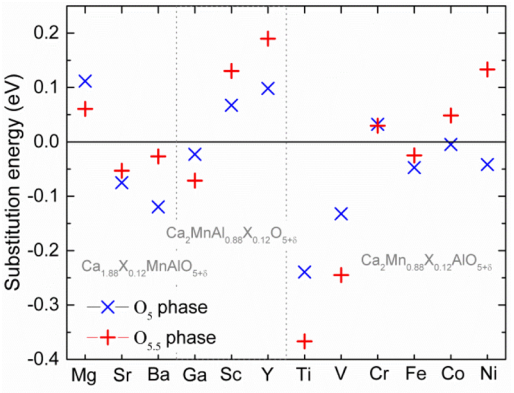

Figure 7. Substitution energies for the doping of $Ca_2MnAlO_{5.5}$ and Ca_2MnAlO_5.

and the $O_{5.5}$ phases. Not all doping strategies are thermodynamically feasible. For instance, Mg doping at the Ca site and Sc or Y doping at the Al site have quite positive substitution energies for both phases. This is easy to understand because the small ionic size of Mg is not enough to fill the large A site in a perovskite-based structure, and the large sizes of Sc and Y are too big for the size requirement of the B site.

The doping of Co and Ni in the O_5 phase is feasible, but their doping in the $O_{5.5}$ phase is energetically unstable. This is due to the large energy cost to oxidize these ions to the 4+ state. The formation of Co^{4+} or Ni^{4+} may even spontaneously induce the release of oxygen in some compounds such as $LiCoO_2$, in which the extraction of Li beyond the composition of $Li_{0.5}CoO_2$ releases oxygen from the lattice.[36] Therefore, for Co- and Ni-doped compounds, the complete oxidation to the formation of the $O_{5.5}$ phase may not be reachable, which implies the decrease of oxygen storage capacity even if the synthesis of doped O_5 phase is still possible.

It is worth noting that the family of Browmillerite compounds contains several distinct crystal structures differing in the relative ordering of the tetrahedral chains between layers and within the layers.[37−39] Although the effect of the crystal structure on the oxygen storage property deserves further comprehensive study, our current work investigates a doping level of 12.5%. It is safe to assume that at this low level, the crystal structure of doped $Ca_2MnAlO_{5+\delta}$ remains similar to that of the parent compound. However, at a higher doping level, the compound may change its crystalline structure. Typically, the DFT method is only capable for searching the local minimum state around the initial configuration. The switch of crystal symmetry may not be captured by the DFT relaxation. To give an example of this, we evaluate the stability of Sr_2MnAlO_5 with different initial configurations. The calculation started with the Ca_2MnAlO_5 structure ends at a local minimum, which is 0.384 eV higher in energy than that started with the experimentally reported Sr_2MnAlO_5 structure (space group *Imma*).[40] There-

DOI: 10.1021/acsami.5b03729
ACS Appl. Mater. Interfaces 2015, 7, 14518−14527

fore, it is important to pay special care when dealing with high doping levels for these compounds.

From the survey in the Inorganic Crystal Structure Database, Ca_2FeAlO_5 is found to be isostructural to Ca_2MnAlO_5. Previous experimental work suggested that it is possible to synthesize the compound $Ca_2Mn_{1-x}Fe_xAlO_5$ in the entire concentration range ($0 \leq x \leq 1$).[15] We examine the formation energy of $Ca_2Mn_{1-x}Fe_xAlO_5$ defined as

$$E_f = E_{Mn_{1-x}Fe_x} - (1-x)E_{Mn} - xE_{Fe} \quad (12)$$

where $E_{Mn_{1-x}Fe_x}$, E_{Mn}, and E_{Fe} are the total energies of $Ca_2Mn_{1-x}Fe_xAlO_5$, Ca_2MnAlO_5, and Ca_2FeAlO_5, respectively.

Figure 8a shows the calculated formation energies for symmetrically distinct $Ca_2Mn_{1-x}Fe_xAlO_5$ configurations. Consistent with the experimental report, nearly all of the calculated formation energies have negative values, suggesting that the formation of $Ca_2Mn_{1-x}Fe_xAlO_5$ solid solution is indeed more stable against the phase separation into a mixture of Ca_2MnAlO_5 and Ca_2FeAlO_5. To assess how the Fe-doping level affects the oxygen storage property, we took the lowest-energy configurations of $Ca_2Mn_{1-x}Fe_xAlO_5$ and calculated the enthalpies for releasing oxygen from their $O_{5.5}$ phases. The reaction enthalpy decreases with Fe content (Figure 8b), suggesting that the oxygen release becomes easier with a higher Fe-doping level. This is in fact not surprising. Because the adsorption of oxygen oxidizes Fe^{3+} to Fe^{4+}, a high concentration of Fe^{4+} should destabilize the oxygen-rich phase and result in a lower reaction enthalpy. To support this, we evaluated the substitutional enthalpy of the O_5 and $O_{5.5}$ phases. For the O_5 phase, the substitutional enthalpy remains negative in the whole composition range. However, for the $O_{5.5}$ phase the substitutional enthalpy rapidly increases with Fe content. It is already positive at 25% of Fe doping, implying that the $O_{5.5}$ phase becomes metastable for this composition. Therefore, too much Fe in $Ca_2Mn_{1-x}Fe_xAlO_5$ should decrease the oxygen storage capacity of this material.

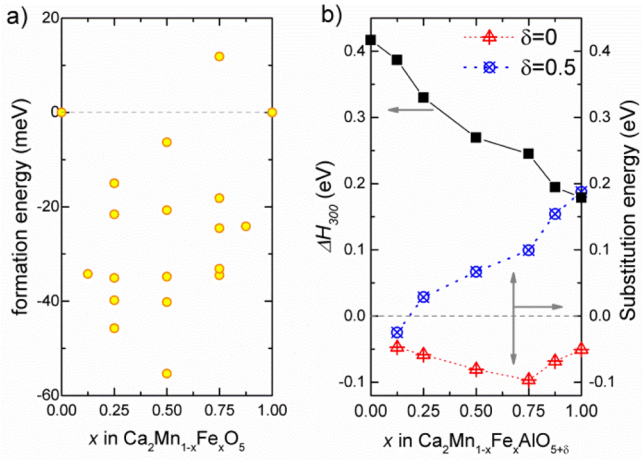

Figure 8. (a) Energies for the formation of symmetrically distinct $Ca_2Mn_{1-x}Fe_xAlO_5$ configurations. (b) Enthalpy for the release of oxygen from $Ca_2Mn_{1-x}Fe_xAlO_{5+\delta}$ and energies for the substitution of Fe for Mn with the formation of $Ca_2Mn_{1-x}Fe_xAlO_{5+\delta}$.

DISCUSSION

In the current work, we perform a comprehensive analysis of the oxygen storage and release property of chemical-doped $Ca_2MnAlO_{5+\delta}$. Obviously, this property is tightly related to the formation of oxygen vacancies in the complex oxide. Oxygen vacancy plays a crucial role in a number of important applications such as solid oxide fuel cells, oxygen separation membranes, and redox oxides. As a topic of great scientific and technologic importance, the chemistry of oxygen vacancy in complex oxides has been the subject of extensive research for decades. It was shown that the formation energetics of isolated oxygen vacancy are well tracked by several first-principles descriptors such as oxygen net charge,[33] band gap,[33,41] oxide formation enthalpy,[41] transition metal−oxygen bond strength,[34] and effective charge of transition metal.[42] Compared to the formation of isolated noninteracting oxygen vacancy, the release of oxygen from $Ca_2MnAlO_{5.5}$ is a more complex process. It involves the formation of multiple interacted oxygen vacancies around Al ions and the reorientation of the oxygen-deficient Al polyhedra into the AlO_4 tetrahedra. Therefore, the current study provides an example by which to analyze the formation energetics of nondilute interacting oxygen vacancy in a complex oxide, which to our knowledge has been rarely carefully investigated before.

On the basis of our calculated data, we examine the correlation between the macroscopic oxygen adsorption enthalpy with several possible quantum chemical descriptors. Early reports showed that the ionic size or the cell volume strongly affects the oxygen release properties.[6,10,11] However, as shown in Figure 9a, for the doping in $Ca_2MnAlO_{5+\delta}$ no apparent correlation exists for any trend. This is probably because the dopants at different sites behave significantly differently. For alkaline earth ion doping at the Ca site, it seems that larger cations expand the lattice and lower the reaction enthalpy. However, for 3d transition metal doping, it is the oxidation of the transition metal that strongly affects the reaction enthalpy instead of the ionic size of the metal. In fact, from Ti to Ni, the ionic size varies very slightly. The ionic size of Ti^{3+} is only 4% larger than that of Mn^{3+}, while Ni^{3+} is 7% smaller. For comparison, Ba^{2+} is 27% larger than Ca^{2+}.[32] Therefore, we may anticipate that the ionic size plays a minor

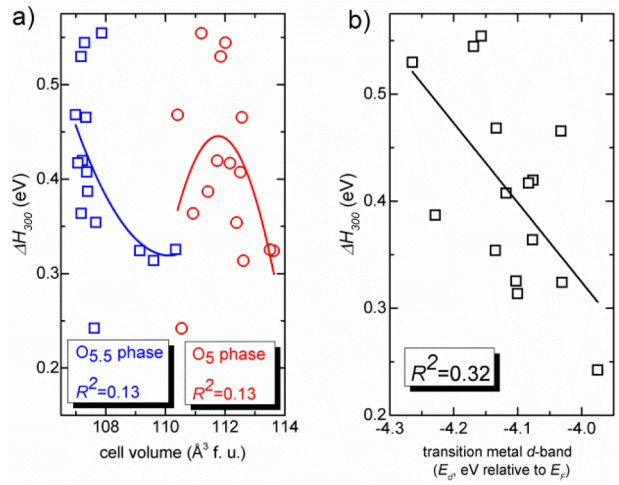

Figure 9. (a) Correlation between the unit cell volume and the enthalpy for the release of oxygen from doped $Ca_2MnAlO_{5.5}$. The solid lines are fitted with parabolic functions. (b) Correlation between the transition metal d-band center and the enthalpy for the release of oxygen from doped $Ca_2MnAlO_{5.5}$.

DOI: 10.1021/acsami.5b03729
ACS Appl. Mater. Interfaces 2015, 7, 14518−14527

role in determining the reaction enthalpy for 3d-transition-metal-doped $Ca_2MnAlO_{5+\delta}$.

Another possible first-principles descriptor is the d-band center of transition metal ions.[43−45] The d-band model works extremely well in describing the catalytic activity of metal catalysts with d-band hybridization with adsorbate s and p orbitals. However, considering the released oxygen does not directly bond with transition metal ions, we may anticipate that the d-band model does not capture the oxygen release property in a complex oxide. As shown in Figure 9b, it seems that a lower d-band position might cause a higher reaction enthalpy, suggesting the difficulty of removing electrons from the lower d-band. However, the quantitative correlation between the reaction enthalpy and the calculated d-band center is quite poor.

Instead of the metal d-band position, here we show that the property for oxygen release in $Ca_2MnAlO_{5.5}$ is well correlated to the p-band position of released oxygen. Figure 10 shows the

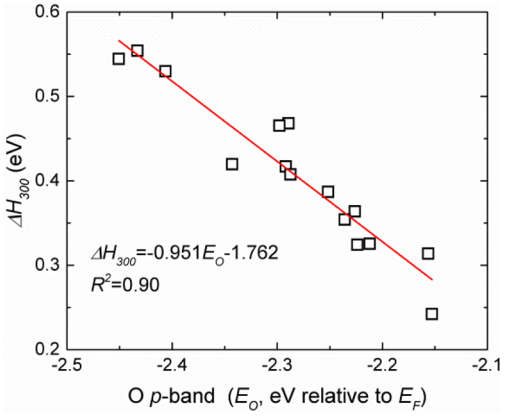

Figure 10. Correlation between the oxygen p-band center relative to the Fermi level and the enthalpy for the release of oxygen from doped $Ca_2MnAlO_{5.5}$. The red line shows the linear fitting to the calculated data.

reaction enthalpy as a function of the oxygen p-band center for the chemical-doped $Ca_2MnAlO_{5.5}$. Remarkably, the reaction enthalpy linearly decreases with oxygen p-band center relative to the Fermi level. A higher-oxygen p-band position leads to lower reaction enthalpy, implying an easier release of oxygen from the oxidized phase. This trend can be interpreted as signifying that the energy to remove electrons from O^{2-} decreases as the oxygen p-band gets closer to the Fermi level. The reaction of 1 oxidizes the half O^{2-} molecule, thus moving one electron from the host oxide. The fitted reaction enthalpy versus the p-band center curve has a slope of −0.951, close to the theoretical value (−1.0).

The nice correlation presented in Figure 10 suggests the chance to tune the O p-band position as a promising strategy to create desirable oxygen storage material for the requirement of different reactions. Previously it was shown that the O p-band center plays an important role in determining the property of perovskite oxides. Lee et al. showed that the O p-band center tracks the formation energy of isolated oxygen vacancy in perovskite $LaBO_3$ with B═Mn, Co, and Ni.[46] They proposed that the oxygen p-band center can be used as a descriptor for the first-principles design of new solid oxide fuel cell cathodes. Grimaud et al. found that the O p-band center nicely correlates the catalytic activity of $(Ln_{0.5}Ba_{0.5})CoO_3$ in the oxygen evolution reaction (OER) with Ln=Ho, Gd, Sm, and Pr.[47] Moving the O p-band center closer to the Fermi level (from $LaCoO_3$ to $(Pr_{0.5}Ba_{0.5})CoO_{3)}$ greatly increases the intrinsic OER activity. However, the stability of oxide in OER decreased if the O p-band center is further lifted. They suggested that the O p-band center is a descriptor for screening the OER activity and stability of oxides. The structure of brownmillerite is a derivative of oxygen-deficient perovskite. It is interesting to see that the O p-band center works remarkably well in this family of compounds. Considering the structure similarity between brownmillerite, perovskite, and double perovskite, we prospect that brownmillerite compounds may show interesting properties in applications such as oxygen reduction and oxygen evolution reaction catalysts.

CONCLUSIONS

To conclude, in the current work we have performed a comprehensive analysis on the oxygen storage and release properties of brownmillerite, $Ca_2MnAlO_{5+\delta}$. Our first-principles calculations reveal that oxygen release from $Ca_2MnAlO_{5.5}$ reduces the coordination around Al ions and switches half-Al from octahedral to tetrahedral bonding. The energy barrier for the migration of oxygen vacancy in $Ca_2MnAlO_{5.5}$ is 0.60−0.62 eV, suggesting remarkable oxygen mobility in this compound. These results agree excellently with experimental observations.

Our results demonstrate that doping $Ca_2MnAlO_{5+\delta}$ is an effective strategy to tune the temperature for oxygen storage and release. For undoped $Ca_2MnAlO_{5+\delta}$, the equilibrium temperature at a pressure of 1 atm of O_2 is 848 K. By the doping of 12.5% of Ga at the Al site and V and Ti at the Mn site, the equilibrium temperature shifts to high values by approximately 110−270 K, while by doping 12.5% of Fe at the Mn site and Sr and Ba at the Ca site, the equilibrium temperature is lowered by approximately 20−210 K. The doping of these elements is thermodynamically stable, while doping other elements including Mg, Sc, Y, Cr, Co, and Ni generates metastable compounds. Doping with a higher Fe content, however, lowers the oxygen storage capacity.

Finally, on the basis of our calculated data, we prove that the formation of nondilute interacting oxygen vacancy in a complex oxide is well correlated to a simple descriptor, the oxygen p-band center. Compounds with oxygen p-band positions closer to the Fermi level have lower oxygen adsorption enthalpies and thus lower equilibrium temperatures between the oxidized and reduced phases. Our results suggest the importance of the O p-band center in the study of perovskite-based compounds. An improved understanding of such fundamental knowledge will pave the road for the future design and optimization of functional oxide materials.

ASSOCIATED CONTENT

Supporting Information

Cartesian coordinates of the relaxed structures of Ca_2MnAlO_5 and $Ca_2MnAlO_{5.5}$ and lattice parameters of binary oxides and Sr_2MnAlO_5. The Supporting Information is available free of charge on the ACS Publications website at DOI: 10.1021/acsami.5b03729.

AUTHOR INFORMATION

Corresponding Author

*E-mail: chen.ling@tema.toyota.com.

DOI: 10.1021/acsami.5b03729
ACS Appl. Mater. Interfaces 2015, 7, 14518−14527

Notes

The authors declare no competing financial interest.

■ ACKNOWLEDGMENTS

The authors are grateful for the discussions with Dr. Paul Fanson. Images of crystal structures were generated with the VESTA program.[48]

■ REFERENCES

(1) Jeen, H.; Choi, W. S.; Biegalski, M. D.; Folkman, C. M.; Tung, I.-C.; Fong, D. D.; Freeland, J. W.; Shin, D.; Ohta, H.; Chisholm, M. F.; Lee, H. N. Reversible Redox Reactions in an Epitaxially Stabilized $SrCoO_x$ Oxygen Sponge. *Nat. Mater.* **2013**, *12*, 1057−1063.

(2) Motohashi, T.; Ueda, T.; Masubuchi, Y.; Takiguchi, M.; Setoyama, T.; Oshima, K.; Kikkawa, S. Remarkable Oxygen Intake/Release Capability of $BaYMn_2O_{5+\delta}$: Applications to Oxygen Storage Technologies. *Chem. Mater.* **2010**, *22*, 3192−3196.

(3) Sugiura, M. Oxygen Storage Materials for Automotive Catalysts: Ceria−Zirconia Solid Solutions. *Catal. Surv. Asia* **2003**, *7*, 77−87.

(4) Kašpar, J.; Fornasiero, P.; Graziani, M. Use of CeO_2-Based Oxides in the Three-Way Catalysis. *Catal. Today* **1999**, *50*, 285−298.

(5) Motohashi, T.; Hirano, Y.; Masubuchi, Y.; Oshima, K.; Setoyama, T.; Kikkawa, S. Oxygen Storage Capability of Brownmillerite-Type $Ca_2AlMnO_{5+\delta}$ and Its Application to Oxygen Enrichment. *Chem. Mater.* **2013**, *25*, 372−377.

(6) Parkkima, O.; Yamauchi, H.; Karppinen, M. Oxygen Storage Capacity and Phase Stability of Variously Substituted $YBaCo_4O_{7+\delta}$. *Chem. Mater.* **2013**, *25*, 599−604.

(7) Baidya, T.; Gayen, A.; Hedge, M. S.; Ravishankar, N.; Dupont, L. Enhanced Reducibility of $Ce_{1-x}Ti_xO_2$ Compared to That of CeO_2 and Higher Redox Catalytic Activity of $Ce_{1-x-y}TixPt_yO_{2-\delta}$ Compared to That of $Ce_{1-x}Pt_xO_{2-\delta}$. *J. Phys. Chem. B* **2006**, *110*, 5262−5272.

(8) Baidya, T.; Hegde, M. S.; Gopalakrishnan, J. Oxygen-Release/Storage Properties of $Ce_{0.5}M_{0.5}O_2$ (M = Zr, Hf) Oxides: Interplay of Crystal Chemistry and Electronic Structure. *J. Phys. Chem. B* **2007**, *111*, 5149−5154.

(9) Baidya, T.; Gupta, A.; Deshpandey, P. A.; Madras, G.; Hegde, M. S. High Oxygen Storage Capacity and High Rates of CO Oxidation and NO Reduction Catalytic Properties of $Ce_{1-x}Sn_xO_2$ and $Ce_{0.78}Sn_{0.2}Pd_{0.02}O_{2-\delta}$. *J. Phys. Chem. C* **2009**, *113*, 4059−4068.

(10) Kadota, S.; Karppinen, M.; Motohashi, T.; Yamauchi, H. R-Site Substitution Effect on the Oxygen-Storage Capability of $RBaCo_4O_{7+\delta}$. *Chem. Mater.* **2008**, *20*, 6378−6381.

(11) Remsen, S.; Dabrowski, B. Synthesis and Oxygen Storage Capacities of Hexagonal $Dy_{1-x}Y_xMnO_{3+\delta}$. *Chem. Mater.* **2011**, *23*, 3818−3827.

(12) Wang, L.; Maxisch, T.; Ceder, G. Oxidation Energies of Transition Metal Oxides within the GGA + U Framework. *Phys. Rev. B: Condens. Matter Mater. Phys.* **2006**, *73*, 195107.

(13) Fultz, B. Vibrational Thermodynamics of Materials. *Progress Mater. Sci.* **2010**, *55*, 247−352.

(14) Collins, C.; Dyer, M. S.; Demont, A.; Carter, P. A.; Thomas, M. F.; Darling, G. R.; Claridge, J. B.; Rosseinsky, M. J. Computational Prediction and Experimental Confirmation of B-Site Doping in $YBa_2Fe_3O_8$. *Chem. Sci.* **2014**, *5*, 1493−1505.

(15) Carvalho, M. D.; Ferreira, L. P.; Waerenborgh, J. C.; Tsipis, E.; Lopes, A. B.; Godinho, M. Structure and Magnetic Properties of $Ca_2Fe_{1-x}Mn_xAlO_{5+d}$. *J. Solid State Chem.* **2008**, *181*, 2530−2541.

(16) Wright, A. J.; Palmer, H. M.; Anderson, P. A.; Greaves, C. Structures and Magnetic Ordering in the Brownmillerite Phases, Sr_2MnGaO_5, and Ca_2MnAlO_5. *J. Mater. Chem.* **2002**, *12*, 978−982.

(17) Palmer, H. M.; Snedden, A.; Wright, A. J.; Greaves, C. Crystal Structure and Magnetic Properties of $Ca_2MnAlO_{5.5}$, an n = 3 Brownmillerite Phase. *Chem. Mater.* **2006**, *18*, 1130−1133.

(18) Kresse, G.; Furthmuller, J. Efficient Iterative Schemes for Ab Initio Total-Energy Calculations Using a Plane-Wave Basis Set. *Phys. Rev. B: Condens. Matter Mater. Phys.* **1996**, *54*, 11169−11186.

(19) Kresse, G.; Hafner, J. Ab Initio Molecular-Dynamics Simulation of the Liquid-Metal−Amorphous-Semiconductor Transition in Germanium. *Phys. Rev. B: Condens. Matter Mater. Phys.* **1994**, *49*, 14251−14269.

(20) Kresse, G.; Joubert, D. From Ultrasoft Pseudopotentials to the Projector Augmented-Wave Method. *Phys. Rev. B: Condens. Matter Mater. Phys.* **1999**, *59*, 1758−1775.

(21) Henkelman, G.; Jónsson, H. Improved Tangent Estimate in the Nudged Elastic Band Method for Finding Minimum Energy Paths and Saddle Points. *J. Chem. Phys.* **2000**, *113*, 9978−9985.

(22) Henkelman, G.; Uberuaga, B. P.; Jónsson, H. A Climbing Image Nudged Elastic Band Method for Finding Saddle Points and Minimum Energy Paths. *J. Chem. Phys.* **2000**, *113*, 9901−9904.

(23) Anderson, M. T.; Vaughey, J. T.; Poeppelmeier, K. R. Structural Similarities among Oxygen-Deficient Perovskites. *Chem. Mater.* **1993**, *5*, 151−165.

(24) Jia, Y.; Jiang, H.; Valkeapää, M.; Yamauchi, H.; Karppinen, M.; Kauppinen, E. I. Oxygen Ordering and Mobility in $YBaCo_4O_{7+\delta}$. *J. Am. Chem. Soc.* **2009**, *131*, 4880−4883.

(25) Motohashi, T.; Ueda, T.; Masubuchi, Y.; Kikkawa, S. Oxygen Intake/Release Mechanism of Double-Perovskite Type $BaYMn_2O_{5+\delta}$ ($0 \le \delta \le 1$). *J. Phys. Chem. C* **2013**, *117*, 12560−12566.

(26) Chroneos, A.; Yildiz, B.; Tarancón, A.; Parfitt, D.; Kilner, J. A. Oxygen Diffusion in Solid Oxide Fuel Cell Cathode and Electrolyte Materials: Mechanistic Insights from Atomistic Simulations. *Energy Environ. Sci.* **2011**, *4*, 2774−2789.

(27) Islam, M. S. Ionic Transport in ABO_3 Perovskite Oxides: a Computer Modelling Tour. *J. Mater. Chem.* **2000**, *10*, 1027−1038.

(28) Parfitt, D.; Chroneos, A.; Kilner, J. A.; Grimes, R. W. Molecular Dynamics Study of Oxygen Diffusion in $Pr_2NiO_{4+\delta}$. *Phys. Chem. Chem. Phys.* **2010**, *12*, 6834−6836.

(29) Gilleßen, M.; Lumeij, M.; George, J.; Stoffel, R.; Motohashi, T.; Kikkawa, S.; Dronskowski, R. Oxygen-Storage Materials $BaYMn_2O_{5+\delta}$ from the Quantum-Chemical Point of View. *Chem. Mater.* **2012**, *24*, 1910−1916.

(30) Grosvenor, A. P.; Greedan, J. E. Analysis of Metal Site Preference and Electronic Structure of Brownmillerite-Phase Oxides ($A_2B'_xB_{2-x}O_5$; A = Ca, Sr; B′/B = Al, Mn, Fe, Co) by X-ray Absorption Near-Edge Spectroscopy. *J. Phys. Chem. C* **2009**, *113*, 11366−11372.

(31) Kuhn, M.; Kim, J. J.; Bishop, S. R.; Tuller, H. L. Oxygen Nonstoichiometry and Defect Chemistry of Perovskite-Structured $Ba_xSr_{1-x}Ti_{1-y}Fe_yO_{3-y/2+\delta}$ Solid Solutions. *Chem. Mater.* **2013**, *25*, 2970−2975.

(32) Shannon, R. D. Revised Effective Ionic Radii and Systematic Studies of Interatomic Distances in Halides and Chalcogenides. *Acta Crystallogr.* **1976**, *A32*, 751−767.

(33) Xiao, P.; Deng, Z. Q.; Manthiram, A.; Henkelman, G. Calculations of Oxygen Stability in Lithium-Rich Layered Cathodes. *J. Phys. Chem. C* **2012**, *116*, 23201−23204.

(34) Pavone, M.; Ritzmann, A. M.; Carter, E. A. Quantum-Mechanics-Based Design Principles for Solid Oxide Fuel Cell Cathode Materials. *Energy Environ. Sci.* **2011**, *4*, 4933−4937.

(35) Waerenborgh, J. C.; Rojas, D. P.; Vyshatko, N. P.; Shaula, A. L.; Kharton, V. V.; Marozau, I. P.; Naumovich, E. N. Fe^{4+} Formation in Brownmillerite $CaAl_{0.5}Fe_{0.5}O_{2.5+\delta}$. *Mater. Lett.* **2003**, *57*, 4388−4393.

(36) Goodenough, J. B.; Kim, Y. Challenges for Rechargeable Li Batteries. *Chem. Mater.* **2010**, *22*, 587−603.

(37) Lambert, S.; Leligny, H.; Grebille, D.; Pelloquin, D.; Raveau, B. Modulated Distribution of Differently Ordered Tetrahedral Chains in the Brownmillerite Structure. *Chem. Mater.* **2002**, *14*, 1818−1826.

(38) D'Hondt, H.; Abakumov, A. M.; Hadermann, J.; Kalyuzhnaya, A. S.; Rozova, M. G.; Antipov, E. V.; Tendeloo, G. V. Tetrahedral Chain Order in the $Sr_2Fe_2O_5$ Brownmillerite. *Chem. Mater.* **2008**, *20*, 7188−7194.

(39) Ramezanipour, F.; Greedan, J. E.; Cranswick, L. M. D.; Garlea, V. O.; Donaberger, R. L.; Siewenie, J. Systematic Study of Compositional and Synthetic Control of Vacancy and Magnetic Ordering in Oxygen-Deficient Perovskites $Ca_2Fe_{2-x}Mn_xO_{5+y}$ and

DOI: 10.1021/acsami.5b03729
ACS Appl. Mater. Interfaces 2015, 7, 14518−14527

$CaSrFe_{2-x}Mn_xO_{5+y}$ (x = 1/2, 2/3, and 1; y = 0−1/2). *J. Am. Chem. Soc.* **2012**, *134*, 3215−3227.
(40) Hadermann, J.; Abakumov, A. M.; D'Hondt, H.; Kalyuzhnaya, A. S.; Rozova, M. G.; Markina, M. M.; Mikheev, M. G.; Tristan, N.; Klingeler, R.; Buechner, B.; Antipov, E. V. Synthesis and Crystal Structure of the $Sr_2Al_{1.07}Mn_{0.93}O_5$ Brownmillerite. *J. Mater. Chem.* **2007**, *17*, 692−698.
(41) Deml, A. M.; Stevanović, V.; Muhich, C. L.; Musgrave, C. B.; O'Hayre, R. Oxide Enthalpy of Formation and Band Gap Energy as Accurate Descriptors of Oxygen Vacancy Formation Energetics. *Energy Environ. Sci.* **2014**, *7*, 1996−2004.
(42) Lee, Y.-L.; Kleis, J.; Rossmeisl, J.; Morgan, D. Ab Initio Energetics of $LaBO_3$ (001) (B = Mn, Fe, Co, and Ni) for Solid Oxide Fuel Cell Cathodes. *Phys. Rev. B: Condens. Matter Mater. Phys.* **2009**, *80*, 224101.
(43) Hammer, B.; Norskov, J. K. Why Gold is the Noblest of All the Metals. *Nature* **1995**, *376*, 238−240.
(44) Norskov, J. K.; Bligaard, T.; Rossmeisl, J.; Christensen, C. H. Towards the Computational Design of Solid Catalysts. *Nat. Chem.* **2009**, *1*, 37−46.
(45) Greeley, J.; Mavrikakis, M. Alloy Catalysts Designed from First Principles. *Nat. Mater.* **2004**, *3*, 810−815.
(46) Lee, Y.-L.; Kleis, J.; Rossmeisl, J.; Shao-Horn, Y.; Morgan, D. Prediction of Solid Oxide Fuel Cell Cathode Activity with First-Principles Descriptors. *Energy Environ. Sci.* **2011**, *4*, 3966−3970.
(47) Grimaud, A.; May, K. J.; Carlton, C. E.; Lee, Y.-L.; Risch, M.; Hong, W. T.; Zhou, J.; Shao-Horn, Y. Double Perovskites as a Family of Highly Active Catalysts for Oxygen Evolution in Alkaline Solution. *Nature Commun.* **2013**, *4*, 2439.
(48) Momma, K.; Izumi, F. VESTA 3 for Three-Dimensional Visualization of Crystal, Volumetric and Morphology Data. *J. Appl. Crystallogr.* **2011**, *44*, 1272−1276.

DOI: 10.1021/acsami.5b03729
ACS Appl. Mater. Interfaces 2015, 7, 14518−14527